NIST Advanced Manufacturing Series
NIST AMS 100-67

Laser Beam Metrology for AM-Bench 2022: Approaches, Results, and Lessons Learned

David Deisenroth
Jordan Weaver
Sergey Mekhontsev
Steven Grantham
Shawn Moylan

This publication is available free of charge from:
https://doi.org/10.6028/NIST.AMS.100-67

NIST NATIONAL INSTITUTE OF STANDARDS AND TECHNOLOGY
U.S. DEPARTMENT OF COMMERCE

NIST Advanced Manufacturing Series
NIST AMS 100-67

Laser Beam Metrology for AM-Bench 2022: Approaches, Results, and Lessons Learned

David Deisenroth
Jordan Weaver
Sergey Mekhontsev
Shawn Moylan
Intelligent Systems Division
Engineering Laboratory

Steven Grantham
Sensor Science Division
Physical Measurement Laboratory

This publication is available free of charge from:
https://doi.org/10.6028/NIST.AMS.100-67

April 2025

U.S. Department of Commerce
Howard Lutnick, Secretary

National Institute of Standards and Technology
Craig Burkhardt, Acting Under Secretary of Commerce for Standards and Technology and Acting NIST Director

NIST AMS 100-67
April 2025

Certain equipment, instruments, software, or materials, commercial or non-commercial, are identified in this paper in order to specify the experimental procedure adequately. Such identification does not imply recommendation or endorsement of any product or service by NIST, nor does it imply that the materials or equipment identified are necessarily the best available for the purpose.

Publication History
Approved by the NIST Editorial Review Board on 2025-03-21

How to Cite this NIST Technical Series Publication
Deisenroth D, Weaver J, Mekhontsev S, Grantham S, Moylan S (2025) Laser Beam Metrology for AM-Bench 2022: Approaches, Results, and Lessons Learned. (National Institute of Standards and Technology, Gaithersburg, MD), NIST Advanced Manufacturing Series (AMS) NIST AMS 100-67. https://doi.org/10.6028/NIST.AMS.100-67

Author ORCID iDs
David Deisenroth: 0000-0002-6869-7970
Jordan Weaver: 0000-0003-4857-5164
Sergey Mekhontsev: 0000-0001-7764-630X
Steven Grantham: 0000-0002-8218-512X
Shawn Moylan: 0000-0003-3927-1118

Contact Information
david.deisenroth@nist.gov

Abstract

One of key parameters of additive manufacturing by laser powder bed fusion of metal parts (PBF-LB/M) is the power density distribution (PDD) of the process laser beam. This paper describes the methods used to measure the beam PDD, discussing well-established metrology of laser beams, and also establishing a reliable location of the build plane in relation to the beam caustic, which is a non-trivial metrology challenge when handling power densities on the order of 10 MW/cm^2. Additionally, several sources of variability of the PDD of nominally axisymmetric Gaussian beams in the PBF-LB/M additive manufacturing environment are discussed. Methods for quantifying measurement uncertainties associated with camera-based beam metrology are also detailed. The sources of variability and measurement uncertainty are then quantified for the specific case of the beam in the NIST Additive Manufacturing Metrology Testbed (AMMT) that was used to generate test artifacts for the 2022 Additive Manufacturing Benchmark Series (AM Bench 2022). The combined statistical variability, measurement uncertainty, and the measured value of the beam diameter are reported for two camera-based instruments as a function of distance relative to the build plane as documentation of the beam caustic used in AM Bench 2022.

Keywords

AM-Bench; laser beam metrology; laser powder bed fusion; metal additive manufacturing; power density distribution metrology

Table of Contents

List of Tables

List of Figures

1. Introduction

Additive manufacturing of metals by laser powder bed fusion (PBF-LB/M) relies on high-power focused laser beams to melt powder to form a part layer by layer. The powder feedstock may be a variety of materials, but this investigation will focus on process parameters (laser power and beam diameter) that are relevant to metal-based PBF-LB/M. Nevertheless, the lessons learned, and the metrological approaches described here may apply to a variety of other high-power laser processing applications.

There are several shapes of power density distribution (PDD) that are industrially relevant for PBF-LB/M, including top hat, ring-shaped beams, and highly elliptic Gaussian beams [1–3]. But, currently, by far the most prevalent PDD for PBF-LB/M is a nominally circular (axisymmetric) Gaussian beam. Circular Gaussian beams are often characterized by a diameter, or "spot size." Two common diameters used in PBF-LB/M are the "Gaussian" (D_g) diameter and the "D4σ" diameter. The Gaussian diameter is the beam diameter at $1/e^2$ (approximately 13.5 %) of the peak intensity. The D4σ is the diameter at which four standard deviations (± 2σ) of the intensity distribution are contained, with equations detailed in ISO 11146-1:2021(which uses the slightly different symbology of d_σ for beam diameter and $d_{\sigma 0}$ for the beam waist diameter) [4]. In an ideal Gaussian beam, the Gaussian and D4σ diameter are identical, and because beams used in PBF-LB/M are typically close to an ideal Gaussian distribution, the two definitions can be used somewhat interchangeably in describing the nominal beam diameter at the build plane. But, it should be noted that the D4σ diameter measurement is highly sensitive to background image level and noise, while the Gaussian curve fit of a nearly Gaussian beam is quite insensitive to a uniform background level. In this work, the Gaussian diameters are reported.

A Gaussian beam used for PBF-LB/M is typically generated by directing a single mode laser through scanning, focusing, and field correction optics. The beam intersects the "build plane" near the beam focus (or beam waist), as illustrated in Fig. 1. In this work, the build plane is assumed to be equivalent to the recoater plane, which is approximately the plane of the top of the powder layer that is ultimately melted by the laser radiation.

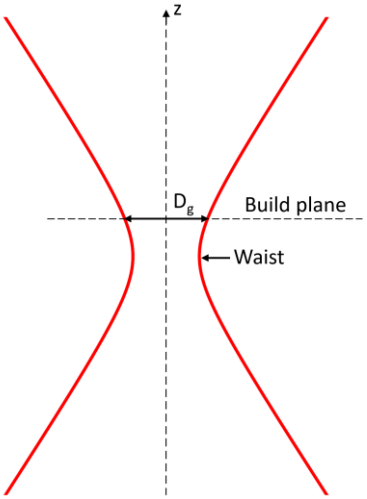

Fig. 1. Illustration of a beam caustic relative to an PBF-LB/M build plane.

Recent studies in metal-based PBF-LB/M indicate that the laser PDD has a strong effect on the properties of the finished parts [5]. Specifically, with commonly used PBF-LB/M materials and process parameters, the relation between melt pool depth generally increases quadratically as the beam diameter is decreased with all other variables held constant [6]. Melt depth is also closely related to the material solidus and sub-solidus cooling rates, and therefore the resulting grain structure and mechanical properties of finished parts.

As such, it has been found that intentionally altering the beam diameter can in some cases be advantageous to the manufacturing process by defocusing the beam to position the waist either above or below the build plane [7]. Conversely, if the beam focus position (and therefore diameter) changes erroneously, the manufacturing process can be adversely affected [8–10]. The diameter can potentially change erroneously by imperfect focusing and/or field correction optics, imperfect alignment with the build plane, thermalization (heat absorption leading to distorted imaging) of the laser optics, and laser window contamination by metal ejecta and/or condensate [11]. The same error sources may also cause the beam to vary from a circular Gaussian profile, which can further adversely affect the manufacturing process. Additionally, the changing incidence angle as the beam moves around the build area can cause beam elongation from a circular profile (ellipticity). And so, this work has sought to quantify each of these sources of beam variability for the case of the AM Bench 2022 laser processing parameters on the Additive Manufacturing Metrology Testbed (AMMT).

In order to quantify each source of beam variation, the beam must be measured, which incurs measurement uncertainty. The challenge in measuring a laser beam used for metal powder bed fusion is that the laser power is on the order of 300 W focused into a beam diameter of only approximately 80 µm, which results in irradiance exceeding 10 MW/cm^2. Devices for measuring the PDD of such high radiant flux beams include scanning pinholes and scanning slits or knife edges that are exposed to the beam for only a short period of time before dissipating any accumulated heat [ISO 13694:2018] [12]. An alternative approach to measuring the high flux beam is to attenuate the power so that it can be imaged with a focal plane array (FPA) camera sensor.

Two complementary attenuation approaches were used in this work. The first approach was to operate the laser in a pulsed mode with a low duty cycle (on the order of 0.1 %) at a power of 100 W. The transmitted power was further reduced by a series of absorptive filters with increasing optical density (OD) that resulted in a total transmission on the order of 1×10^{-10} (OD 10) in the collimated portion of the beam before the scanning and focusing/field correction optics. The highly attenuated beam was then focused directly on to the FPA, resulting in an image of the beam distribution at the build plane. For this application, a windowless FPA (WFPA) was used to eliminate any assumptions about the thickness and refractive index of cover glass (which nearly all cameras have) over the FPA. A laser distance finder (manufacturer stated maximum error of ± 2.5 µm) was used to precisely locate the WFPA relative to the build plane, which resulted in a measurement approach of the attenuated beam that required minimal assumptions. The deficiency of this PDD measurement approach is that it does not image the beam with full power passing through the laser optics.

The second PDD measurement approach implemented a beam splitter that sampled the full power beam approximately 70 mm above the build plane. The integrated WFPA imaged a very small fraction of the beam power (comparable to that in the previous approach) reflected off of the beam splitter. The metrological challenge with this approach is that the optical path distance from the beam splitter to the build plane and from the beam splitter to the integrated WFPA must be calibrated very accurately. In this work, the optical path distance was calibrated against the standalone WFPA with an estimated standard measurement uncertainty (Type B, k = 1) of 200 µm of the beam imaging position. This calibration also requires the reasonable assumption that the beam diameter does not change appreciably due to thermalization of the optics in the first 33 ms of laser operation at full power.

The two camera-based PDD measurement approaches are complimentary because of their differing capabilities. The standalone WFPA can measure the beam around the build area with no optical path distance calibration required, while the beam splitter device intercepts the beam at full power at normal incidence in the build area. The two instruments are further complimentary because the two WFPAs had differing pixel pitches. The pixel pitch of the standalone WFPA was 5.5 µm/pixel and the pixel pitch of the beam splitter integrated WFPA was 3.69 µm/pixel. The effect of pixel pitch will be discussed in the measurement uncertainty section.

The remainder of this publication is organized into four main sections. First, quantification of the beam non-idealities is detailed. Second, uncertainties associated with measuring the beam are discussed. Third, the combined uncertainty of the beam diameter are tabulated, and the beam caustic that was used for the AM Bench 2022 single line, pad, and 3-dimensional (3D) build tests is plotted [13]. Finally, the summary and future work section will describe the lessons learned and future direction.

2. Uncertainty components due to a non-ideal beam

A variety of simplifications are required when characterizing a focused laser beam by a single (Gaussian) diameter. The beam power density distribution deviates from an axisymmetric (circular) profile, varies around the build area, varies temporally, and changes with window contamination. Derivation of each uncertainty component associated with representing a non-ideal beam with a single diameter is described in the following subsections.

2.1. Deviation from a circular profile

Imperfect laser optics, including the collimator, diverging and converging lens, scanning mirrors, and windows can combine to create a non-circular beam at the build plane. Defocusing the beam (moving the beam waist downward relative to the build plane) can exacerbate the non-circularity, as shown in Fig. 2. As shown, the beam is closest to an ideal circle ($\varepsilon \geq 0.95$) with a spot diameter of 67 µm to 77 µm. The ellipticity drops below the ISO 11146-1:2021 value for treatment as a circular beam ($\varepsilon \geq 0.87$) only at the extremes of the nominal diameter range of 44 µm and 131 µm. It should be noted that optimized commercial machines are likely to have a much more circular profile than exhibited by the AMMT when these measurements were taken, so these values should not be taken as representative of commercial machine performance. Error bars are omitted from Fig. 2 because the spot size is to be represented by a single diameter value and ellipticity is treated as a deviation from the nominal value. These are values of the major and minor diameter averaged with cold laser optics.

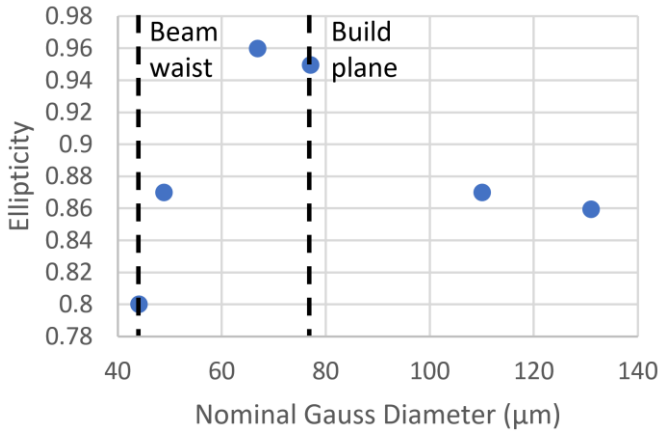

Fig. 2. Beam ellipticity as a function of nominal spot diameter at normal beam incidence at the center of the build area.

These data are taken at normal incidence at the center of the build area and 285 W power delivered to the beam splitter device. The standard uncertainty associated with treating the beam as circular when it is actually ellipsoidal was found by calculating the root-mean squared error (RMSE) in the radius of an ellipse from that of the radius of an equivalent area circle in 10° increments, as exemplified in Fig. 3. The following subsection will describe the effects of moving the beam around the build area.

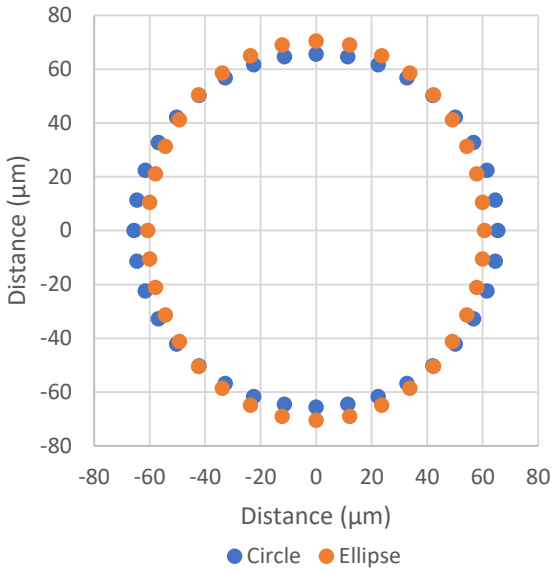

Fig. 3. Elliptic profile (ε = 0.86) compared with a circular profile with 10° increments.

2.2. Variability around the build area

As the laser is moved around the build area, the nominal diameter varies because of imperfect compensation of the dynamic focusing lens. Additionally, the ellipticity may change across the build area because of the change in incidence angle away from the center position. In order to measure this effect, and collapse the variability into a single value of deviation from ideal, the WFPA was aligned to the build plane and translated about the plane to measure the beam major and minor diameter at 25 locations distributed around the build area. The standard deviation of the 50 spot diameters (major and minor at 25 locations) was then taken, resulting in a relative standard uncertainty due to translation around the build area of 3.4 %. As may be expected, ellipticity tended to increase near the perimeter of the build area due to the higher angle of beam incidence.

2.3. Temporal variation due to heated optics

As described previously, projecting the beam directly onto a WFPA requires a very low laser duty cycle with high attenuation, in order to remain under the damage threshold and within the dynamic range of the imager. This results in passing less than 1 mW through the laser optics, which is not a realistic representation of the thermal load, and therefore does not capture any thermal effects on the optics. Thus, the full laser power must be passed through the optics into the build chamber and then sampled.

In the case study of interest (AM Bench 2022), the laser power was 285 W and the duty cycle of a typical layer was approximately 50 %. Tests were performed to assess optical heating and focus shift resulting from a typical layer scanned at 285 W with a duty cycle of 50 % (the

majority of layers had duty cycles between 40 % and 60 %) compared with steady and static application of 150 W, and it was found that the two were comparable. It was also found that the optics cool to nearly the starting temperature in the recoating time by thermally loading the optics comparably to a typical layer, then pausing for the recoating duration, and then reloading the optics comparably to a typical layer. The starting and ending spot diameter of each layer were approximately equivalent after three layers, and so heat accumulation throughout a 3D build was found to be of little concern. Fig. 4 illustrates the temporal variation in nominal spot diameter due to optics heating and focus shift over the course of a typical AM Bench 2022 3D build layer.

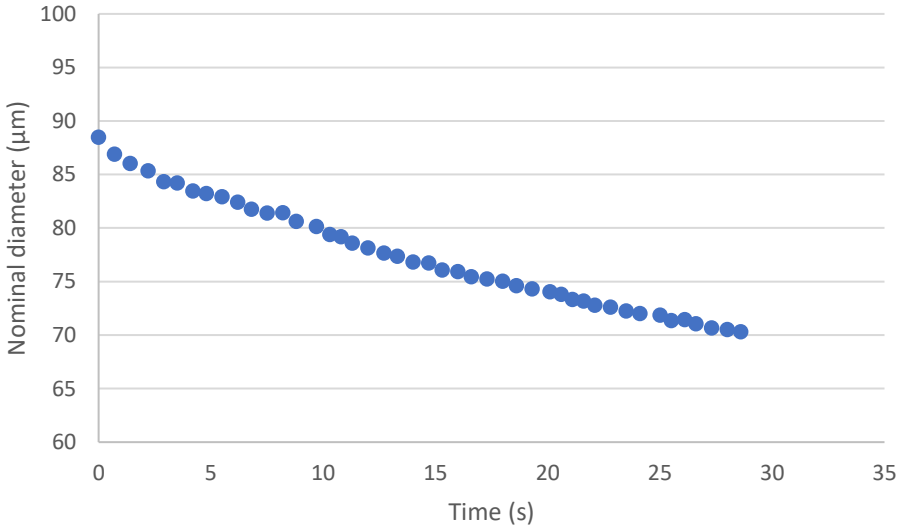

Fig. 4. Nominal beam diameter as a function of time with 150 W steady power at normal incidence, representative of a thermal load imposed by a typical AM Bench 2022 layer.

During 3D builds, the spot size was set such that the average spot size on a typical layer would be approximately 77 µm. Because the spot size variation is systematic with time and the scan position is known as a function of time for each layer, the nominal spot size could theoretically be mapped to position for each layer. But, given the magnitude of other uncertainties, such complex treatment is unnecessary. And so, the average spot diameter is used, and the temporal standard deviation is the associated measurement uncertainty component, which is 5.0 µm. It should again be noted that optimized commercial machines are likely to have much more stable optical performance than was exhibited by the AMMT when these measurements were taken.

2.4. Window contamination

The spot size variability caused by passing a full power laser through a laser window that has been contaminated by ejecta and condensate during an approximately 6 hr long 3D build was assessed by measuring diameter before and after. Because these measurements were repeated in such a close timeframe, they are treated as uncorrelated with measurement repeatability. The resulting spot diameter uncertainty component due to window contamination during 3D

builds is 0.8 µm for the case of AM Bench 2022. It should be noted, though, that if left unattended, the window contamination can become a major source of beam variability. The combined uncertainty in diameter due to measurement uncertainties is summarized in the following section.

3. Measurement uncertainty components

The following subsections detail the uncertainty components associated with spot diameter measurement. The components include pixelation and noise, curve fit error, measurement reproducibility, and vertical misalignment of the metrology. Note that the bit depth resolution can be considered negligible compared to other uncertainty components because the 12-bit detector results in a 'binning' effect of less than 0.03 %.

3.1. Pixelation and noise

The combined effects of pixelation and noise on the fit diameter was modeled computationally. First, an array with at least 22 × 22 supersampling (uniformly subdividing) of each pixel is generated to create a good approximation (0.001% curve fit error from the input Gaussian profile) of a simulated Gaussian beam profile, as illustrated in Fig. 5a. Next, the simulated radiance profile was 'pixelated' by averaging the supersampled grid across the area of each pixel. Then, a Gaussian noise distribution with σ = 2 % (calculated typical transient pixel noise of the WFPA) of the local pixel value was applied to the simulated pixel array, as illustrated in Fig. 5b.

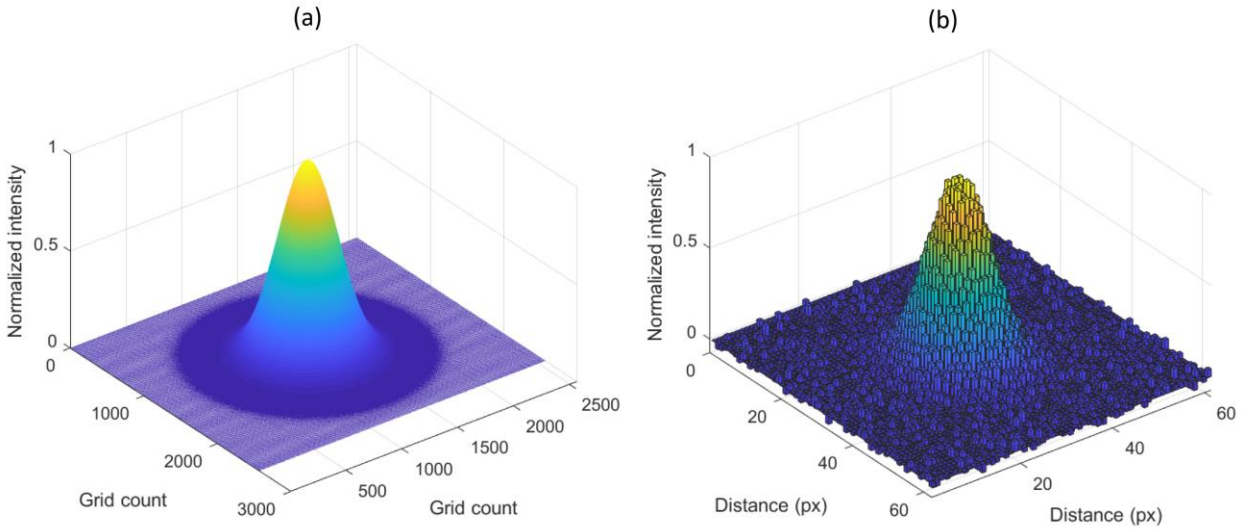

Fig. 5. (a) simulated beam profile generated by a supersampled array representing at least 22 × 22 subdivisions of each pixel and (b) simulated measurement profile generated by averaging the simulated radiance profile across each pixel and adding Gaussian noise.

The simulated signal array was then fit with a 2-dimensional Gaussian curve and the simulated 'measured' major and minor diameters were found. This process was repeated with the peak of the simulated radiance profile positioned in a 6 x 6 evenly spaced array within the central (peak) pixel to quantify the effect of the Gaussian peak position relative to the pixel array. The average of the 36 output diameters then established the final set of 'measured' major and minor diameters that were compared with the input diameters of the original Gaussian profile. These processes were then repeated for each nominal diameter (and associated ellipticity) of

interest. The computed measurement error for two pixel pitches representative of the WFPA and beam splitter device are summarized in Fig. 6.

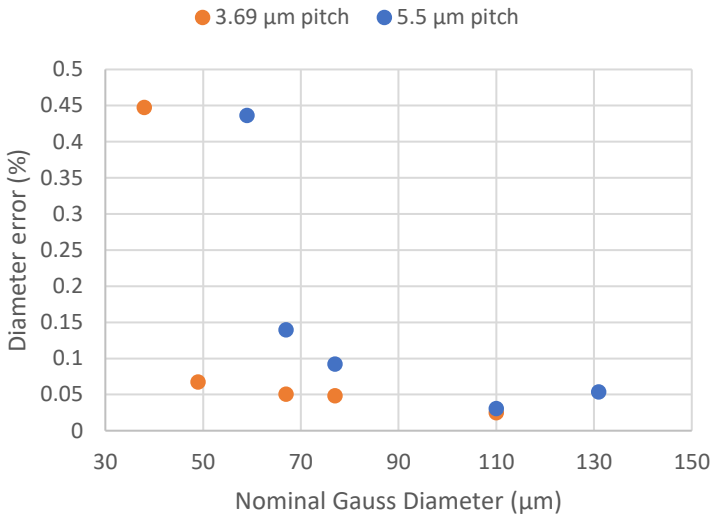

Fig. 6. Computed measurement error due to pixelation and noise.

As shown in Fig. 6, the relative measurement error increases as the diameter decreases because the signal is convolved onto fewer and fewer pixels. If the nominal diameter falls below approximately 10× the pixel pitch, the measurement results become inconsistent and sometimes nonphysical, which means that under this limit pixelation may become the dominant measurement uncertainty. The following subsection addresses the measurement uncertainty associated with fitting a 2-dimensional curve to a non-ideal Gaussian distribution.

3.2. Curve fit error

The radiance profile received by the WFPA deviates slightly from an ideal Gaussian, as illustrated in Fig. 7. The diameter measurement uncertainty associated with curve fit error is found by calculating the RMSE between the 2-dimensional curve fit and the measured pixel values, giving the error in 'intensity' or relative pixel value. The RMSE is then divided by the local slope of the curve fit at the Gaussian diameter level (approximately 13.5% of the peak), which converts the value from 'intensity' to diameter distance units. The standard relative measurement uncertainty associated with curve fitting (u_{RSME}) was found to have a typical value of 0.5 %. This process is illustrated in the lower right corner of Fig. 7. Measurement repeatability is discussed in the following subsection.

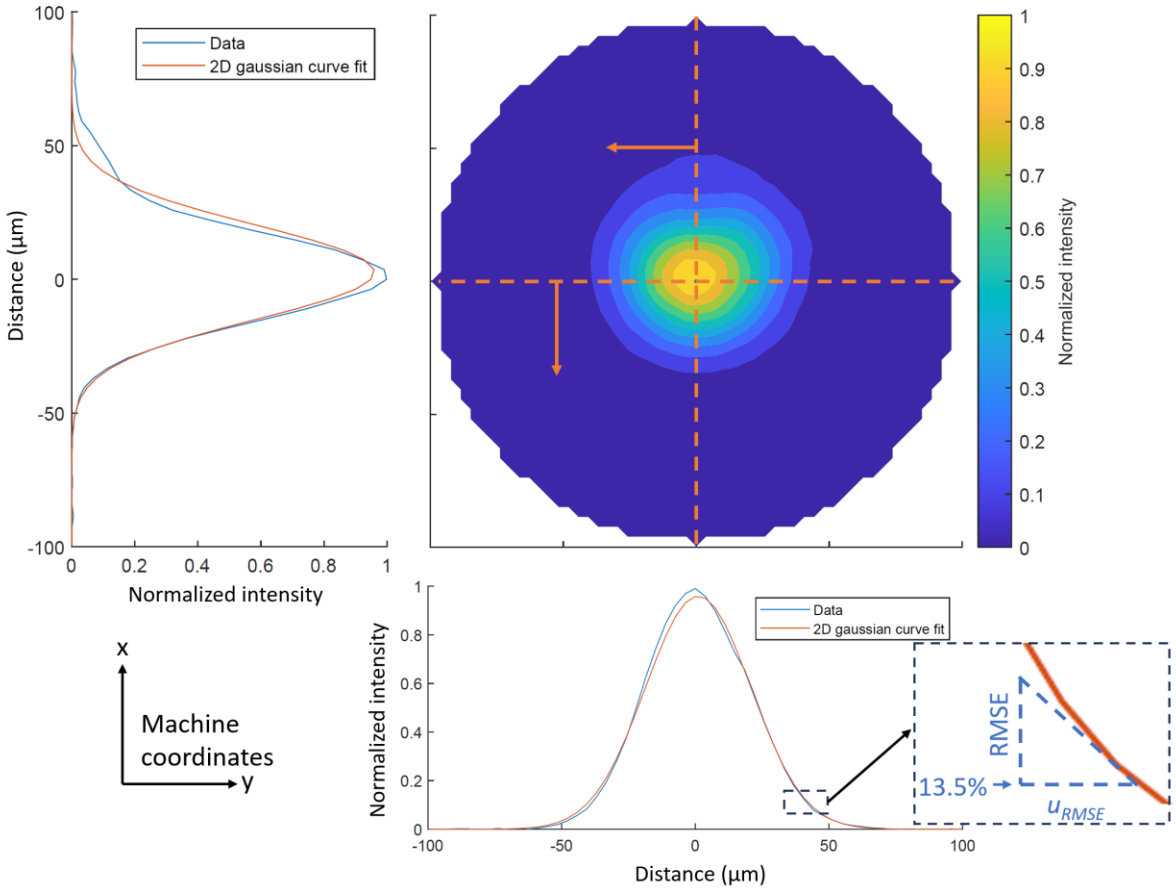

Fig. 7. Normalized signal intensity as a function of position with x and y-direction central cross sections. Calculation of the standard relative measurement uncertainty associated with curve fitting (u_{RMSE}) is illustrated in the lower right corner.

3.3. Measurement repeatability

The spot diameter was measured on five separate occasions over the course of approximately one year. The standard deviation of the nominal diameter was 3.1 %. Because the sample size is relatively low, a t-factor is taken from a student's t table for a confidence interval of 68.3 %, resulting in t = 1.14. This additional coverage factor is then multiplied by the standard deviation, resulting in a relative standard measurement uncertainty associated with repeatability of 3.5 %. The measurement uncertainty associated with vertical misalignment of the measurement device is described in the following subsection.

3.4. Z-position uncertainty

Although vertical misalignment of the measurement device to the build plane may be correlated with measurement repeatability, it was found that the effect of the misalignment was small compared with repeatability, and so the two uncertainty components are treated as uncorrelated. The standard deviation of vertical misalignment is approximately 20 µm. This value is found with 22 samples with a laser distance finder manufacturer stated maximum error of ± 2.5 µm. This value is then divided by the local slope of the beam caustic to find the diameter measurement uncertainty, similar to the method described in Section 3.2 for curve fit error. At more than approximately one Rayleigh length (distance at which the beam diameter is $\sqrt{2}\times$ the beam waist diameter) from the beam waist, the beam diverges linearly, and the measurement uncertainty takes on a constant value of 0.7 µm. But, near the beam waist where the diameter is very slowly changing along the beam axis, the measurement uncertainty becomes only 0.2 µm due to vertical misalignment.

4. Combined spot diameter uncertainty

Each standard uncertainty (k = 1) component is calculated as described in the preceding sections. Then, the combined uncertainties (u_A) of D_g are calculated with the RSME equation, where $u^2(x_i)$ are normal-distribution standard uncertainties for each uncertainty component:

$$u_A(D_g) = \sqrt{\sum_{i=1}^{n} u^2(x_i)}$$

The uncertainty in position relative to the build plane is based on empirical repeatability of positioning the WFPA with a laser distance finder, with a standard measurement uncertainty (Type A) of ± 20 µm. The plate that the beam splitter device rested on has the same positioning uncertainty as the WFPA. This uncertainty is root-sum squared with the optical path distance uncertainty (described in Section 1), resulting in a standard positioning uncertainty of ± 201 µm.

The following subsection summarizes the effect of each uncertainty component on the combined diameter uncertainty for the AM Bench 2022 single line and pad tests. In the single line and pad tests, optics heating and window contamination do not significantly affect the spot size because of the short duration of the tests. Also, a variety of spot diameters were used in the single line and pad tests, and so each diameter of interest is detailed. The second subsection details the additional uncertainties associated with AM Bench 2022 3D builds at the nominal 3D spot diameter.

4.1. Single line and pad tests

As shown in Table 1, the measurement uncertainty associated with pixelation and noise is the smallest component for each spot size. But, it must be noted that pixelation can become the largest uncertainty component in the case of measurement of nominal beam diameters of less than approximately 10× the pixel pitch. The second and third smallest uncertainty components for all diameters are curve fit error and vertical misalignment, respectively. At each nominal diameter, the uncertainty component of variation around the build area is slightly larger than the measurement repeatability component (3.4 % compared to 3.1 %). At diameters of 44 µm, 49 µm, 110 µm, and 131 µm, the largest uncertainty component is deviation from a circular profile due to the greater ellipticity. At diameters of 67 µm, 77 µm, and 97 µm, the largest uncertainty component is variation around the build area. Similarly, the smallest combined relative diameter uncertainty is exhibited with diameters of 67 µm, 77 µm, and 97 µm, while the largest combined relative uncertainties are exhibited at the two smallest and two largest diameters.

Table 1. Standard uncertainty (k = 1) components and combined uncertainty as a function of nominal beam diameter

Nominal beam diameter (µm)	Unc. Type	44	49	67	77	97	110	131
Deviation from a circular profile (µm)	A	3.4	2.4	1	1.4	2.7	5.3	6.9
Variation around the build area (µm)	A	1.5	1.7	2.3	2.6	3.3	3.7	4.5
Pixelation and noise (µm)	A	0.19	0.03	0.07	0.07	0.05	0.04	0.07
Curve fit error (µm)	A	0.2	0.2	0.3	0.4	0.5	0.6	0.6
Measurement repeatability (µm)	A	1.5	1.7	2.3	2.7	3.4	3.9	4.6
Vertical misalignment (µm)	A	0.2	0.5	0.7	0.7	0.7	0.7	0.7
Combined standard uncertainty (µm)		**4.0**	**3.3**	**3.3**	**3.9**	**5.3**	**7.4**	**9.2**
Combined relative standard uncertainty (%)		**9.2**	**7.0**	**5.2**	**5.3**	**5.7**	**6.9**	**7.2**

The measured diameter as a function of vertical position D(z) relative to the build plane (caustic) and associated uncertainties are shown graphically in Fig. 8. As stated previously, the WFPA is not used to measure beam diameters at or below 55 µm, but the smaller pixel pitch of the beam splitter allows for diameter measurements in this range. A hyperbolic curve fit (of all of the data) per ISO 11146-1:2021 is supplied for reference, which is representative of the nominal beam profile for the AM Bench 2022 single line and pad tests, as well as the 3D builds. But, note that the diameter uncertainty is greater due to 3D build conditions, which will be discussed in the following subsection.

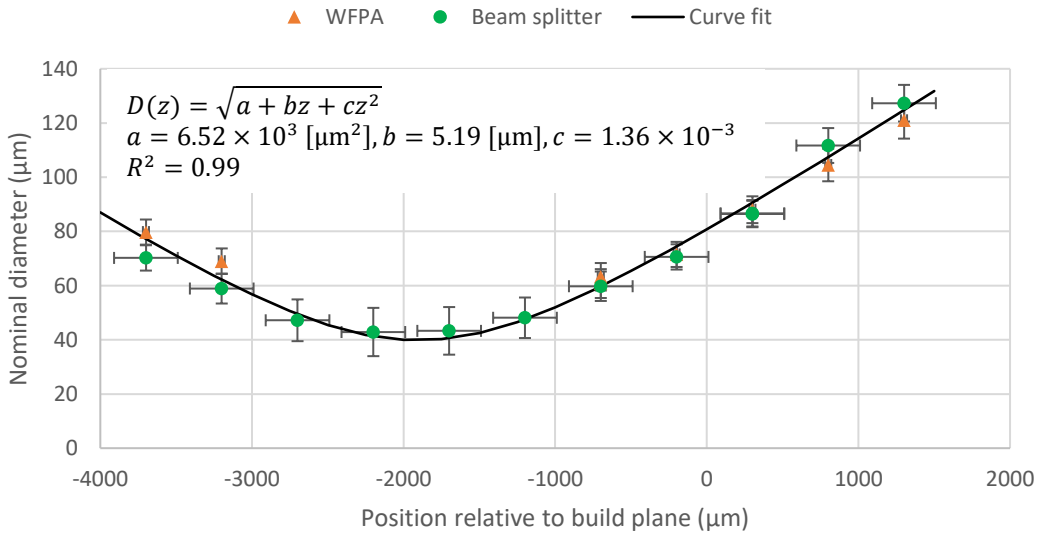

Fig. 8. Beam caustic measured with two devices (beam splitter pixel pitch was 3.69 µm and WFPA pixel pitch was 5.5 µm) with a representative hyperbolic curve fit, $D_g(z)$.

4.2. 3D builds

The diameter uncertainty components associated with the nominal 3D build diameter are tabulated in Table 2. The first six uncertainty components are the same for the 3D build as the 77 µm single line and pad test diameters shown in Table 1. But, the additional components of temporal variation due to heated optics, and window contamination become important in the 3D build environment. It was found that window contamination became a moderate uncertainty component, while temporal variation became the largest diameter uncertainty component.

Table 2: Standard uncertainty (k = 1) components and combined uncertainty as a function of nominal beam diameter

Nominal beam diameter (µm)	Unc. Type	77
Deviation from a circular profile (µm)	A	1.4
Variation around the build area (µm)	A	2.6
Temporal variation due to heated optics (µm)	A	5.0
Window contamination (µm)	A	0.8
Pixelation and noise (µm)	A	0.1
Curve fit error (µm)	A	0.4
Measurement repeatability (µm)	A	2.4
Vertical misalignment (µm)	A	0.7
Combined standard uncertainty (µm)		**6.4**
Combined relative standard uncertainty (%)		**8.3**

5. Summary and future work

This study documents the nominal beam diameter, associated beam variability, and the measurement uncertainty of the NIST AMMT for the AM Bench 2022 processing environment. In this work, the beam profile is nominally circular and the Gaussian diameter ($1/e^2$) of the beam is reported.

Sources of beam variability included deviation from a circular profile, variability around the build area, temporal variation due to heated optics, and laser window contamination. In the case of the AMMT at the AM Bench 2022 processing parameters, it was found that for the single line and pad tests, the largest beam variability sources were ellipticity and beam variability around the build area. The largest source of beam variability in the 3D build tests was due to the temporal variation due to heated optics. It should be noted that the relative magnitude of each variability component in this case is not necessarily representative of the laser diameter variability in commercial systems. For instance, window contamination can often become the largest source of beam variability in commercial PBF-LB/M systems.

Two camera-based instruments with differing attenuation optics and laser settings were used in this study. The sources of beam measurement uncertainty included pixelation and noise, curve fit error, measurement repeatability, and vertical misalignment of the measurement instruments. In this study, it was found that measurement repeatability was the largest source of measurement uncertainty of the nominal beam diameter. But, it should also be noted that when attempting to measure a beam diameter of less than approximately 10× the pixel pitch, pixelation may become the dominant measurement uncertainty. The combined relative standard (k = 1) diameter uncertainty in this study was found to range from 5.0 % to 9.0 % based on nominal diameter value, which ranged from 44 µm to 131 µm.

Future work includes more accurate calibration of beam splitter optical path distances, exploring smaller pixel pitch imagers with greater imaging frequencies, as well as other approaches for measuring the beam diameter at off-normal incidence. Finally, metrology, data processing, and result interpretation approaches will be investigated for non-Gaussian beam profiles.

References

[1] Sow MC, De Terris T, Castelnau O, Hamouche Z, Coste F, Fabbro R, Peyre P (2020) Influence of beam diameter on Laser Powder Bed Fusion (L-PBF) process. *Additive Manufacturing* 36:101532. https://doi.org/10.1016/j.addma.2020.101532

[2] Roehling TT, Shi R, Khairallah SA, Roehling JD, Guss GM, McKeown JT, Matthews MJ (2020) Controlling grain nucleation and morphology by laser beam shaping in metal additive manufacturing. *Materials & Design* 195:109071. https://doi.org/10.1016/j.matdes.2020.109071

[3] Grünewald J, Gehringer F, Schmöller M, Wudy K (2021) Influence of Ring-Shaped Beam Profiles on Process Stability and Productivity in Laser-Based Powder Bed Fusion of AISI 316L. *Metals* 11(12). https://doi.org/10.3390/met11121989

[4] ISO (2021) *11146-1 – Lasers and laser-related equipment — Test methods for laser beam widths, divergence angles and beam propagation ratios* (ISO).

[5] Weaver JS, Heigel JC, Lane BM (2022) Laser spot size and scaling laws for laser beam additive manufacturing. *Journal of Manufacturing Processes* 73:26–39. https://doi.org/10.1016/j.jmapro.2021.10.053

[6] Naderi M, Weaver J, Deisenroth D, Iyyer N, McCauley R (2023) On the Fidelity of the Scaling Laws for Melt Pool Depth Analysis During Laser Powder Bed Fusion. *Integrating Materials and Manufacturing Innovation* 12(1):11–26. https://doi.org/10.1007/s40192-022-00289-w

[7] Metelkova J, Kinds Y, Kempen K, de Formanoir C, Witvrouw A, Van Hooreweder B (2018) On the influence of laser defocusing in Selective Laser Melting of 316L. *Additive Manufacturing* 23:161–169. https://doi.org/10.1016/j.addma.2018.08.006

[8] Aggarwal A, Patel S, Kumar A (2019) Selective Laser Melting of 316L Stainless Steel: Physics of Melting Mode Transition and Its Influence on Microstructural and Mechanical Behavior. *JOM* 71(3):1105–1116. https://doi.org/10.1007/s11837-018-3271-8

[9] Berez J, Dushaj E (2023) Additive manufacturing machine tool qualification: Methods and insights. *Joint Special Interest Group meeting between euspen and ASPE Advancing Precision in Additive Manufacturing* (KU Leuven, Belgium).

[10] Berez J, Dushaj E, Jost E, Saldaña C, Fu K (2024) Measurement of focal plane error in laser powder bed fusion machines. *Additive Manufacturing Letters* 9:100196. https://doi.org/10.1016/j.addlet.2024.100196

[11] Anping Liu, Kefeng Li (2021) Thermal lensing mitigation for high power laser processing. *High-Power Laser Materials Processing: Applications, Diagnostics, and Systems X (SPIE LASE)*, Vol. 11679, p 116790L. https://doi.org/10.1117/12.2578360

[12] ISO (2018) *13694 – Optics and photonics — Lasers and laser-related equipment — Test methods for laser beam power (energy) density distribution* (ISO).

[13] Levine L, Lane B, Becker C, Belak J, Carson R, Deisenroth D, Glaessgen E, Gnaupel-Herold T, Gorelik M, Greene G, Habib S, Higgins C, Hill M, Hrabe N, Killgore J, Kim JW, Lemson G, Migler K, Moylan S, Pagan D, Phan T, Praniewicz M, Rowenhorst D, Schwalbach E, Seppala J, Simonds B, Stoudt M, Weaver J, Yeung H, Zhang F (2024) Outcomes and Conclusions from the 2022 AM Bench Measurements, Challenge Problems, Modeling

Submissions, and Conference. *Integrating Materials and Manufacturing Innovation* 13(3):598–621. https://doi.org/10.1007/s40192-024-00372-4